Research Article Vol. 7, No. 7 | 1 Jul 2017 | OPTICAL MATERIALS EXPRESS 2477

Optical Materials EXPRESS

Conformal spray-deposited fluorine-doped tin oxide for mid- and long-wave infrared plasmonics

RICKY GIBSON,[1,2,*] **SHIVASHANKAR VANGALA,**[2,3] **ISAIAH O. OLADEJI,**[4] **EVAN SMITH,**[2,5] **FARNOOD KHALIZADEH-REZAIE,**[6] **KEVIN D. LEEDY,**[2] **BRUCE CLAFLIN,**[2] **TIM COOPER,**[2,5] **ROBERT E. PEALE,**[6] **AND JUSTIN W. CLEARY**[2]

[1]*University of Dayton Research Institute, Dayton, OH 45469, USA*
[2]*Air Force Research Laboratory, Sensors Directorate, Wright-Patterson AFB, OH 45433, USA*
[3]*Azimuth Corporation, Dayton, OH 45341, USA*
[4]*SISOM Thin Films LLC, Orlando, FL 32805, USA*
[5]*KBRWyle, Beavercreek, OH 45431, USA*
[6]*Department of Physics, University of Central Florida, Orlando, FL 32816, USA*
**rgibson1@udayton.edu*

Abstract: Nanocrystalline spray-deposited fluorine-doped tin oxide (FTO) was investigated for mid- and long-wave infrared plasmonics. Silicon lamellar gratings were conformally coated with FTO, and the excitation of surface plasmon polaritons (SPP) was investigated via their angle and wavelength-dependent reflectivity. Photon-to-SPP coupling efficiency as a function of grating parameters, and in comparsion to gallium-doped zinc oxide (GZO) gratings, was quantitatively analyzed based on a figure of merit related to the sharpness and depth of the coupling resonance. Conformal spray-deposited FTO would be useful in mid- and long-wave infrared plasmonic channel wave guides.

OCIS codes: (240.6680) Surface plasmons; (250.5403) Plasmonics; (130.3060) Infrared; (310.7005) Transparent conductive coatings; (160.4670) Optical materials; (280.4788) Optical sensing and sensors.

References and links

1. M. Kanehara, H. Koike, T. Yoshinaga, and T. Teranishi, "Indium tin oxide nanoparticles with compositionally tunable surface plasmon resonance frequencies in the near-IR region," J. Am. Chem. Soc. **131**(49), 17736–17737 (2009).
2. G. T. Papadakis and H. A. Atwater, "Field-effect induced tunability in hyperbolic metamaterials," Phys. Rev. B **92**(18), 184101 (2015).
3. G. V. Naik, J. Liu, A. V. Kildishev, V. M. Shalaev, and A. Boltasseva, "Demonstration of Al:ZnO as a plasmonic component for near-infrared metamaterials," Proc. Natl. Acad. Sci. U.S.A. **109**(23), 8834–8838 (2012).
4. A. K. Pradhan, R. M. Mundle, K. Santiago, J. R. Skuza, B. Xiao, K. D. Song, M. Bahoura, R. Cheaito, and P. E. Hopkins, "Extreme tunability in aluminum doped zinc oxide plasmonic materials for near-infrared applications," Sci. Rep. **4**(1), 6415 (2015).
5. J. W. Cleary, M. R. Snure, K. D. Leedy, D. C. Look, K. Eyink, and A. Tiwari, "Deterministic IR surface plasmon properties in doped zinc oxides," Proc. SPIE **8545**, 85450 (2012).
6. M. S. Allen, J. W. Allen, B. R. Wenner, D. C. Look, and K. D. Leedy, "Application of highly conductive ZnO to the excitation of long-range plasmons in symmetric hybrid waveguides," Opt. Eng. **52**(6), 064603 (2013).
7. L. Dominici, F. Michelotti, T. M. Brown, A. Reale, and A. Di Carlo, "Plasmon polaritons in the near infrared on fluorine doped tin oxide films," Opt. Express **17**(12), 10155–10167 (2009).
8. F. Khalilzadeh-Rezaie, I. O. Oladeji, J. W. Cleary, N. Nader, J. Nath, I. Rezadad, and R. E. Peale, "Fluorine-doped tin oxides for mid-infrared plasmonics," Opt. Mater. Express **5**(10), 2184–2192 (2015).
9. S. Law, V. Podolskiy, and D. Wasserman, "Towards nano-scale photonics with micro-scale photons: the opportunities and challenges of mid-infrared plasmonics," Nanophotonics **2**(2), 103–130 (2013).
10. R. E. Peale, E. Smith, H. Abouelkhair, I. O. Oladeji, S. Vangala, T. Cooper, G. Grzybowski, F. Khalilzadeh-Rezaie, and J. W. Cleary, "Electrodynamic properties of aqueous spray deposited SnO_2:F films for infrared plasmonics," Opt. Eng. **56**(3), 037109 (2017).
11. R. R. West, S. Ishii, G. Naik, N. Emani, V. M. Shalaev, and A. Boltasseva, "Searching for better plasmonic materials," Laser Photonics Rev. **4**(6), 795–808 (2010).

#291130 https://doi.org/10.1364/OME.7.002477
Journal © 2017 Received 29 Mar 2017; revised 20 May 2017; accepted 20 May 2017; published 16 Jun 2017

12. E. Feigenbaum, K. Diest, and H. A. Atwater, "Unity-order index change in transparent conducting oxides at visible frequencies," Nano Lett. **10**(6), 2111–2116 (2010).
13. R. Soref, R. E. Peale, and W. Buchwald, "Longwave plasmonics on doped silicon and silicides," Opt. Express **16**(9), 6507–6514 (2008).
14. O. D. Miller, A. G. Polimeridis, M. T. Homer Reid, C. W. Hsu, B. G. DeLacy, J. D. Joannopoulos, M. Soljačić, and S. G. Johnson, "Fundamental limits to optical response in absorptive systems," Opt. Express **24**(4), 3329–3364 (2016).
15. H. Matsui, A. Ikehata, and H. Tabata, "Asymmetric plasmon structures on ZnO: Ga for high sensitivity in the infrared range," Appl. Phys. Lett. **109**(19), 191601 (2016).
16. S. Herminjard, L. Sirigu, H. P. Herzig, E. Studemann, A. Crottini, J.-P. Pellaux, T. Gresch, M. Fischer, and J. Faist, "Surface Plasmon Resonance sensor showing enhanced sensitivity for CO2 detection in the mid-infrared range," Opt. Express **17**(1), 293–303 (2009).
17. S. Q. Li, P. Guo, L. Zhang, W. Zhou, T. W. Odom, T. Seideman, J. B. Ketterson, and R. P. H. Chang, "Infrared plasmonics with indium-tin-oxide nanorod arrays," ACS Nano **5**(11), 9161–9170 (2011).
18. M. Abb, Y. Wang, N. Papasimakis, C. H. de Groot, and O. L. Muskens, "Surface-enhanced infrared spectroscopy using metal oxide plasmonic antenna arrays," Nano Lett. **14**(1), 346–352 (2014).
19. J. Kim, A. Dutta, B. Memarzadeh, A. V. Kildishev, H. Mosallaei, and A. Boltasseva, "Zinc oxide based plasmonic multilayer resonator: Localized and gap surface plasmon in the infrared," ACS Photonics **2**(8), 1224–1230 (2015).
20. I. M. Pryce, Y. A. Kelaita, K. Aydin, and H. A. Atwater, "Compliant metamaterials for resonantly enhanced infrared absorption spectroscopy and refractive index sensing," ACS Nano **5**(10), 8167–8174 (2011).
21. L. Labadie, P. Kern, P. Labeye, E. Lecoarer, C. Vigreux-Bercovici, A. Pradel, J.-E. Broquin, and V. Kirschner, "Technology challenges for space interferometry: The option of mid-infrared integrated optics," Adv. Space Res. **41**(12), 1975–1982 (2008).
22. S. Zhu, G. Q. Lo, and D. L. Kwong, "Electro-absorption modulation in horizontal metal-insulator-silicon-insulator-metal nanoplasmonic slot waveguides," Appl. Phys. Lett. **99**(15), 151114 (2011).
23. S. Zhu, G. Q. Lo, and D. L. Kwong, "Phase modulation in horizontal metal-insulator-silicon-insulator-metal plasmonic waveguides," Opt. Express **21**(7), 8320–8330 (2013).
24. J. W. Cleary, R. Gibson, E. M. Smith, S. Vangala, I. O. Oladeji, F. Khalilzadeh-Rezaie, K. Leedy, and R. E. Peale, "Infrared photonic to plasmonic couplers using spray deposited conductive metal oxides," Proc. SPIE **10105**, 101050 (2017).
25. J. W. Cleary, N. Nader, K. D. Leedy, and R. Soref, "Tunable short- to mid-infrared perfectly absorbing thin films utilizing conductive zinc oxide on metal," Opt. Mater. Express **5**(9), 1898–1909 (2015).
26. J. R. Hendrickson, S. Vangala, N. Nader, K. Leedy, J. Guo, and J. W. Cleary, "Plasmon resonance and perfect light absorption in subwavelength trench arrays etched in gallium-doped zinc oxide film," Appl. Phys. Lett. **107**(19), 191906 (2015).
27. N. Nader, S. Vangala, J. R. Hendrickson, K. D. Leedy, D. C. Look, J. Guo, and J. W. Cleary, "Investigation of plasmon resonance tunneling through subwavelength hole arrays in highly doped conductive ZnO films," J. Appl. Phys. **118**(17), 173106 (2015).
28. G. V. Naik, and A. Boltasseva, "Semiconductors for plasmonics and metamaterials," Phys. Status Solidi Rapid Res. Lett. **295–297**(10), 1–7 (2010).
29. C. Rhodes, S. Franzen, J.-P. Maria, M. Losego, D. N. Leonard, B. Laughlin, G. Duscher, and S. Weibel, "Surface plasmon resonance in conducting metal oxides," J. Appl. Phys. **100**(5), 054905 (2006).
30. S. A. Maier, *Plasmonics: Fundamentals and Applications* (Springer Science & Business Media, 2007).
31. L. C. Botten, M. S. Craig, R. C. McPhedran, J. L. Adams, and J. R. Andrewartha, "The finitely conducting lamellar diffraction grating," J. Mod. Opt. **28**(8), 1087–1102 (1981).
32. L. C. Botten, M. S. Craig, and R. C. McPhedran, "Highly conducting lamellar diffraction gratings," J. Mod. Opt. **28**(8), 1103–1106 (1981).
33. I. R. Hooper and W. L. Barnes, "The Basics of Plasmonics," *Handbook of Surface Science*, Vol. 4, N.V. Richardson and Stephen Holloway, eds. (North-Holland, 2014). Chapter 2, pp. 37–74.
34. L. Rayleigh, "On the dynamical theory of gratings," Proc. R. Soc. Lond., A Contain. Pap. Math. Phys. Character **79**(532), 399–416 (1907).
35. A. Savitzky and M. J. E. Golay, "Smoothing and differentiation of data simplified least squares procedures," Anal. Chem. **36**(8), 1627–1639 (1964).
36. Lumerical Solutions, Inc., http://www.lumerical.com/tcad-products/fdtd/
37. R. G. Gordon, "Criteria for choosing transparent conductors," MRS Bull. **25**(08), 52–57 (2000).
38. F. Khalilzadeh-Rezaie, C. J. Fredericksen, W. R. Buchwald, J. W. Cleary, E. M. Smith, I. Rezadad, J. Nath, P. Figueiredo, M. Shahzad, J. Boroumand, M. Yesiltas, G. Medhi, A. Davis, and R. E. Peale, "Planar integrated plasmonic mid-IR spectrometer," MRS Proceedings, **1510** (2013).
39. V. E. Babicheva, A. Boltasseva, and A. V. Lavrinenko, "Transparent conducting oxides for electro-optical plasmonic modulators," Nanophotonics **4**(1), 165–185 (2015).
40. Y. Zhong, S. D. Malagari, T. Hamilton, and D. Wasserman, "Review of mid-infrared plasmonic materials," J. Nanophotonics **9**(1), 093791 (2015).
41. G. V. Naik, V. M. Shalaev, and A. Boltasseva, "Alternative plasmonic materials: beyond gold and silver," Adv. Mater. **25**(24), 3264–3294 (2013).

1. Introduction

Transparent conductive oxides (TCOs) have been shown to be promising hosts for infrared surface plasmon polaritons (SPP). These TCOs include indium tin oxide (ITO) [1, 2], aluminum-doped zinc oxide (AZO) [3, 4], gallium-doped zinc oxide (GZO) [5, 6], fluorine-doped tin oxide (FTO) [7, 8], and antimony-doped tin oxide (ATO) [1]. Properties of SPPs on these TCOs, and localized surface plasmon resonances (LSPRs) in TCO nanoparticles have been studied, but mainly in the near-infrared (NIR). This paper investigates mid-wave infrared (MWIR) and long-wave infrared (LWIR) SPPs on FTO in comparison to GZO. FTO is best suited for plasmonic chemical and bio sensing applications, filters, and emitter enhancement in the MWIR and LWIR [9]. Its highest demonstrated plasma frequency corresponds to a wavelength of 1.9 μm, which is beyond the telecommunications range [10].

TCO plasmonic properties can be tuned during fabrication [5, 10, 11] and actively post-fabrication [2, 4, 12]. TCOs confine the infrared SPPs more tightly to the metal/dielectric interface than do typical metals. Their CMOS compatibility would make TCOs appealing as infrared plasmonic waveguides [13]. TCOs can be formed as nano- and micro-structures, such as nanorods, to optimize infrared plasmonic applications [14]. TCOs have been shown to be useful for sensing applications in the NIR and short-wave IR [15] as well as for MWIR-to-LWIR sensing applications [16–20] and for integrated optics [21–23].

This paper reports the MWIR and LWIR plasmonic properties of FTO. Photonic-to-plasmonic coupling is demonstrated using FTO lamellar gratings. This coupling is compared to that for GZO gratings. The merits and practical considerations for plasmonics of using conformal spray deposited FTO are discussed.

2. Experimental details

Lamellar gratings with 50% duty cycle were fabricated from silicon by photolithography and reactive ion etching (RIE) (SF_6/O_2 chemistry, etch rate of ≈0.66 μm/min). The resulting grating sidewalls have a 1.19 μm radius of curvature. Gratings with period Λ_{MWIR} = 10 μm and Λ_{LWIR} = 20 μm were fabricated, so that first and negative-third order resonances could be investigated over the MWIR and LWIR, respectively. The optimal coupling was determined to occur for a grating height of 0.84 μm [24], which is the value chosen for the gratings studied here.

The silicon gratings were over-coated with optically thick FTO or GZO films. For FTO gratings, the silicon was first coated with 10 nm of SiO_2 deposited by plasma-enhanced chemical vapor deposition (PECVD) to make them hydrophyllic. FTO was then grown by the aqueous spray method called Streaming Process for Electrodeless Electrochemical Deposition (SPEED) [8, 10] at 480°C. A F/Sn ratio of 15% in the precursor solution had been previously determined to give the highest conductivity [10]. The scanning electron microscopy (SEM) images in Fig. 1(a) and 1(b) show a conformal coating with a measured thickness of 0.610 μm.

GZO films of 1.16 μm thickness were pulsed-laser-deposited (PLD) on Si lamellar gratings using KrF excimer laser and ZnO with 0.5 wt % Ga_2O_3 target. SEM images are presented in Fig. 1(c) and 1(d). MWIR and LWIR tunable plasmonic properties of GZO have been well-studied already [25–27]. PLD provided blanket coatings resulting in a comparable optically thick profile to the conformal spray-deposited FTO coating. Optical properties of PLD GZO films are well correlated with deposition conditions [5], allowing reliable comparison to spray deposited FTO.

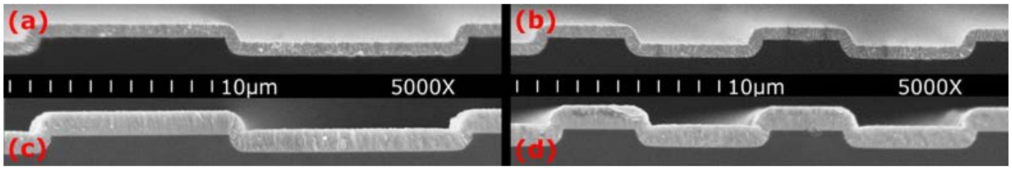

Fig. 1. SEM images at a magnification of 5000X for (a) 20 μm period FTO, (b) 10 μm period FTO, (c) 20 μm period GZO, and (d) 10 μm period GZO gratings.

For measurement of optical constants, films were deposited on unpatterned wafers under the same deposition conditions described above for gratings. These smooth films were characterized using a J.A. Woollam IR-VASE ellipsometer from 1.5 to 40 µm wavelength. A smooth PLD GZO film using a ZnO target with 3 wt. % Ga_2O_3 was also prepared. For convenience, we will refer to the two GZO samples as lo-GZO and hi-GZO for the 0.5% and 3% PLD targets, respectively.

Final grating duty cycles were extracted from cross-section SEM images at the half-height of the grating. For the 20 µm (10 µm) grating period this resulted in a duty cycle of 47.3% and 48.9% (45.7% and 46.8%) for the FTO and GZO gratings, respectively. The resulting m = 1 and m = –3 SPP resonances have similar strength and are present for both LWIR (Λ = 20 µm) and MWIR (Λ = 10 µm) allowing for a more direct comparison over the full spectral range of interest. Even order resonances are very weak, as expected for gratings with nearly 50% duty cycle due to the lack of even Fourier harmonics.

To study the SPP coupling characteristics of the gratings, specular reflection is measured using a Huber dual-angle goniometer where the first stage rotates the sample to scan the angle of incidence (θ), and the second stage controls the detector angle (2θ), both within an accuracy of 0.01°. The source for the MWIR is a Daylight Solutions MIRcat which houses four quantum cascade lasers (QCLs) covering a wavelength range from 3.96 to 5.96 µm. For the LWIR a Daylight Solutions Uber-Tuner QCL, which is tunable from 7.9 µm to 10.5 µm, is used. Both laser sources are pulsed at 100 kHz frequency with a 500 ns pulse width and a 5% duty cycle. A Daylight Solutions HgCdTe detector along with a Zurich Instruments UHFLI lock-in amplifier are used for detection. The incident beam on the grating is TM polarized. All reflectance data is normalized to reflectance spectra of a sputter deposited 300 nm thick gold mirror collected under the same experimental conditions.

3. Measurements

The measured complex permittivity data for the smooth films are presented in Fig. 2. The zero-crossing of the FTO film falls between that of the two GZO films. The permittivity spectra for the FTO (black) and lo-GZO (blue) follow the same trend, while hi-GZO (grey) has a more rapidly decreasing ε' beyond $\lambda \approx 6$ µm and a more rapidly increasing ε'' beyond $\lambda \approx 8$ µm. The crossover wavelengths where ε' becomes negative are 1.92, 2.45, and 1.46 µm for FTO, lo-GZO, and hi-GZO, respectively. Comparison of the FTO SPP resonances to those for the two GZO samples whose plasma frequencies bracket that of the FTO sample allows for fairer comparison of the two materials. Doping level controls permittivity for FTO and GZO [10, 5], as for other TCOs [28, 29].

Figure 2 also presents spectra of the relevant lengths that characterize SPPs out to λ = 12 µm. The calculated characteristic lengths are from the ellipsometry data of the conductors shown in Fig. 2 with air as the dielectric medium. The FTO and GZO films have similar SPP intensity propagation lengths,

$$L_x = \left[2\,\mathrm{Im}(k_{SPP})\right]^{-1} \tag{1}$$

where the SPP wavevector k_{SPP} is found from the dielectric and conductor permittivity spectra, $\varepsilon_{d,c}$, according to

$$k_{SPP} = \frac{2\pi}{\lambda}\sqrt{\frac{\varepsilon_d \varepsilon_c}{\varepsilon_d + \varepsilon_c}}\ . \tag{2}$$

SPPs on hi-GZO propagate farther at the cost of worse field confinement L_d in the dielectric compared to the other films, where

$$L_{d,c} = \left[\frac{2\pi}{\lambda}\mathrm{Re}\left(\sqrt{\frac{-\varepsilon_{d,c}^2}{\varepsilon_d + \varepsilon_c}}\right)\right]^{-1}. \tag{3}$$

Electrical properties (resistivity, mobility, and carrier concentration) of all three films are compared in Table 1. X-ray photoelectron spectra (XPS) measurements were used to determine the dopant concentrations in the doped films. Hall Effect measurements were completed using an Accent Optical Technologies system in the Van der Pauw configuration. Contactless rf-eddy-current method (Lehighton Electronics, Inc.) was used to extract the resistivity, ρ (sheet resistance multiplied by the film thickness). The FTO and lo-GZO films have similar resistivity.

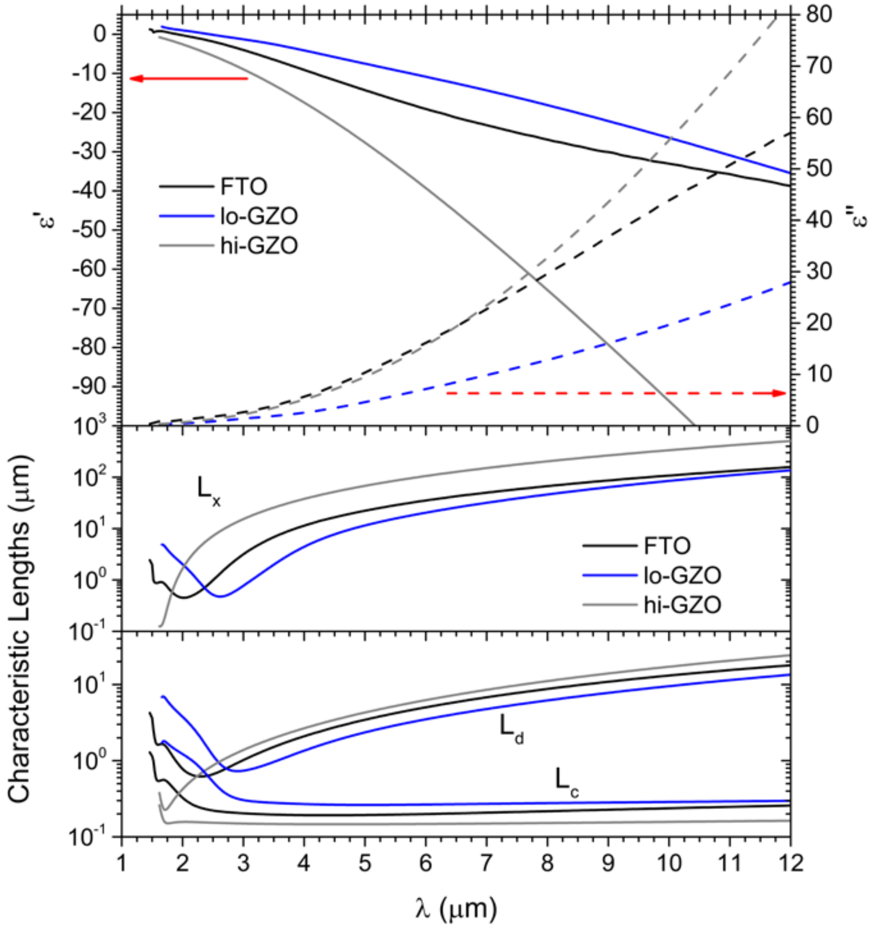

Fig. 2. Measured complex permittivities for FTO (black), lo-GZO (blue), hi-GZO, (grey) films along with the corresponding characteristic lengths for SPPs calculated from complex permittivities with a dielectric medium of air.

Table 1. Electrical Properties of FTO and GZO

Material	Source Dopant Concentration	Actual Dopant Concentration	ρ (mΩ•cm)	μ (cm^2/V•s)	N (10^{20} cm^{-3})
FTO	20% (solution)	1.0%	0.86	15.3	4.76
lo-GZO	0.5 wt. %	0.5%	0.85	30.6	2.39
hi-GZO	3 wt. %	2.9%	0.20	32.9	9.35

The SPP excitation occurs when wavelength and incidence angle satisfy the SPP coupling condition [30],

$$\mathrm{Re}\left[k_{SPP}\right]\mathrm{sign}(m)=\frac{2\pi}{\lambda}\left[\sin\theta+\frac{m\lambda}{\Lambda}\right]. \tag{4}$$

The SPP excitation in the LWIR that meets the criteria of Eq. (4) for an idealized FTO grating, i.e. rectangular profile, are shown in Fig. 3. The strength of the specular reflection of Fig. 3 matches well with the measured data to be described in Fig. 4 in both amplitude and location. A couple even orders are observed due to the rectangular profile and the deviation from a 50% duty cycle described in the previous section. Further details of the corresponding FDTD simulations are described below.

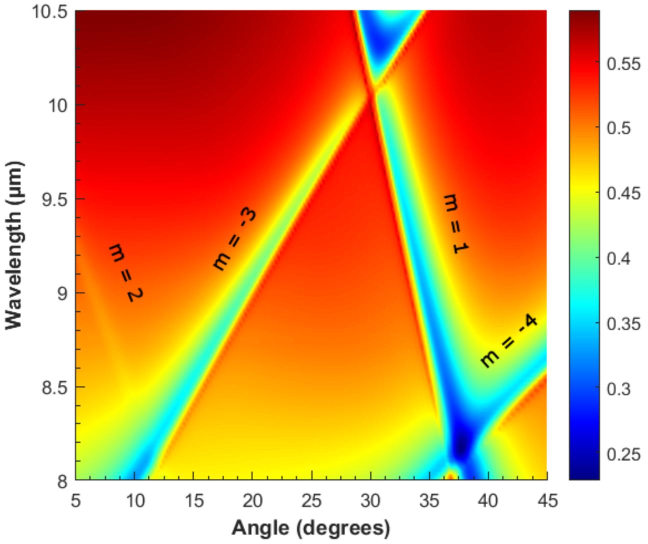

Fig. 3. Simulated specular reflection of a FTO grating (Λ_{LWIR} = 20 µm) with duty cycle matching the fabricated structures but with a rectangular profile. Even orders are stronger than seen in experiment due to the rectangular profile.

Angular reflectance spectra are plotted in Fig. 4. The first (m = 1) and negative-third (m = –3) order SPP excitation resonances in LWIR (MWIR) for 20 (10) µm period gratings are indicated in the top (bottom) portion of Fig. 4. FTO and lo-GZO data are presented on the left and right sides of Fig. 4, respectively. Several spectra have been smoothed to compensate for low signal-to-noise ratio at wavelengths of weak QCL intensity. For both grating periods, m = –3 increases in angle, and m = 1 decreases in angle, with increasing wavelength. The symbols in Fig. 4 represent predicted resonance angles from Eq. (4). In the LWIR, the FTO and lo-GZO resonances have very similar resonance shape and strength. In the MWIR, the resonances on the FTO grating tend to be sharper and better defined due to the higher plasma frequency.

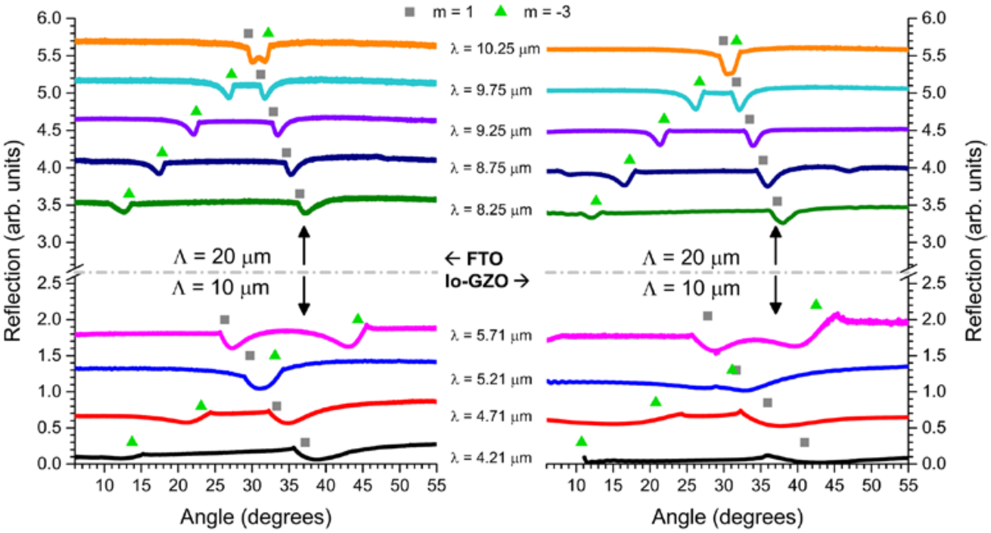

Fig. 4. Angular spectra of FTO grating (left) and lo-GZO grating (right). The grey dashed line separates the different grating periods, Λ = 20 μm (top) and 10 μm (bottom). Each spectrum is offset vertically by 0.5 and corresponds to a different wavelength as indicated. The calculated SPP excitation resonances from Eq. (4) are represented by symbols for m = 1 or m = –3, as indicated.

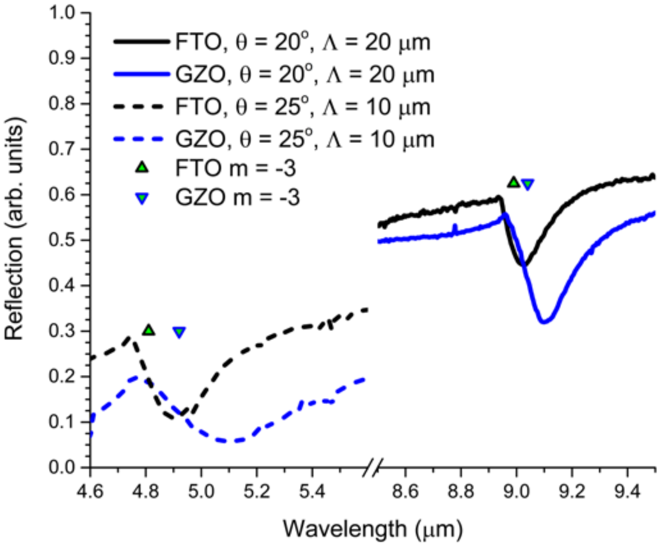

Fig. 5. Wavelength sweep comparison of the m = –3 resonance for 1% FTO (black) and 0.5% GZO (blue). Green triangles represent the calculated location of the SPP excitation. MWIR (dashed lines) spectra are at an angle of incidence of 25° with a grating period of 10 μm and the LWIR spectra (solid lines) are at an angle of 20° with a grating period of 20 μm.

Figure 5 presents the m = –3 resonance in more detail to show that the lo-GZO resonances are somewhat (significantly) broader in the LWIR (MWIR). The m = –3 resonance was chosen for comparison in Fig. 5 because it falls within the central wavelength range for both the MWIR and LWIR experiments at a similar angle which experimentally presents the fairest comparison of broadening with respect to the two ranges. The ε' values are more similar in the LWIR, but the ε'' values more similar in the MWIR. Thus, the ε' values have a larger role in resonance line shape. The offset of the reflectivity baseline for the gratings is consistent with the difference in the reflectivity for the two materials at a given wavelength. The depth of the resonances with respect to the baseline is related to the grating height and grating shape. The grating height controls when critical coupling occurs, where the energy transfer from the photonic mode to the plasmonic mode is highest. This condition depends on permittivity and the grating profile determines the energy distribution between the different m-order resonances.

4. Analysis

Calculation of the asymmetric resonance line shapes requires a complicated formalism for metallic lamellar gratings of rectangular profile [31, 32]. However, several key features can be interpreted using a simpler model for a sinusoidal grating profile. Then, the angular reflectivity of the SPP is given by

$$R = 1 - \frac{4\gamma_r\gamma_i}{\left(k_{SPP}^2 - k_x^2\right)^2 + \left(\gamma_r + \gamma_i\right)^2}. \qquad (5)$$

where k_x is the in-plane component of the photon excitation wavevector and γ_i & γ_r are the intrinsic and radiative damping, respectively [33]. Radiative damping depends on grating height, while the intrinsic damping is determined by the material, grating profile, and defects. Ignoring the latter, and for a given grating profile, intrinsic damping decreases as the SPP intensity propagation length and field penetration depth increase with increasing wavelength. The sharpest linewidth occurs when γ_r is minimized, which occurs when the grating height is zero [33]. However, coupling strength diminishes with reduced grating height. Strongest (critical) coupling of incident light to SPPs occurs when the reflectivity in Eq. (5) goes to zero, which occurs when intrinsic and radiative damping are equal and the coupling condition in Eq. (4) is met.

The Eq. (5) line shape is symmetric in k_x about k_{SPP}, and since the resonance occurs in a fairly narrow range of angles, the line shape would be nearly the same if it were plotted in terms of incidence angle. However, Eq. (5) is for SPPs only and does not include the change in reflected energy caused by a diffracted beam, of the same order m, disappearing as it passes through an exit angle of 90° [34]. This effect is responsible for the sharp edges seen in the experimental data for positive (negative) orders on the lower (higher) angle side of the SPP resonance. These edges complicate the analysis of the line strength and width. To avoid this problem, we introduce a new figure of merit (FOM), namely the magnitude of the derivative of the reflectance spectra with respect to angle. The derivative of R with respect to incidence angle is first negative and then flips sign and becomes positive at resonance as the resonance is approached from below. The sharper and deeper the line, the larger the peak-to-peak amplitude of the derivative. Thus, narrowing and deepening of the resonance each cause the FOM to increase.

Derivatives of measured data were taken after the data were interpolated to give even point spacing. Savitzky-Golay smoothing with a second order polynomial over twenty data points was used, and the final evenly spaced points were separated by 0.001625 degrees [35]. Derivatives of simulated spectra were also obtained for comparison. Simulations were done using the built-in grating analysis tool in Lumerical FDTD Solutions [36] for an idealized lamellar grating evenly coated with 0.61 μm of the respective conducting oxide. The angular resolution of the simulations was 0.1 degrees. Derivatives were again taken using Savitzky-Golay smoothing over three simulated data points with a second order polynomial.

Typical derivative spectra are presented in Fig. 6 (a) for the first order resonance on FTO grating with a 20 μm period to illustrate the processing to arrive at the FOM. The m = 1 resonance was chosen for presentation in Fig. 6 (a) because it remains within a convenient angular range over the full wavelength range of the LWIR QCL and has the best signal-to-noise ratio. The measured and simulated results are in good agreement for the LWIR range. MWIR simulation results are not included in Fig. 6 because they agree poorly with experiment. This is because the assumption of perfectly rectangular gratings for the simulations is a poor representation of the fabricated gratings at these shorter wavelengths and grating periods, so that the relative strengths of different observed orders, or strengths of the Fourier harmonics, differs from those of the simulation. Simulation based on actual grating profile confirms the measured MWIR lineshapes, but would be much more computationally intense to complete for all wavelengths and both materials.

Figure 6 (b) presents derivative FOM for all gratings and resonances of Fig. 4 and for the LWIR simulated spectra. The FTO gratings have higher FOM for both orders in both wavelength ranges. The FOM increases with wavelength as the conductive oxides become electrodynamically better conductors. Outliers occur where resonance orders cross (5.21 to 5.46 µm wavelengths). For the negative-third order on the FTO grating the crossing leads to an increase in the derivative FOM while for both orders of the GZO grating it isn’t possible to distinguish the resonances.

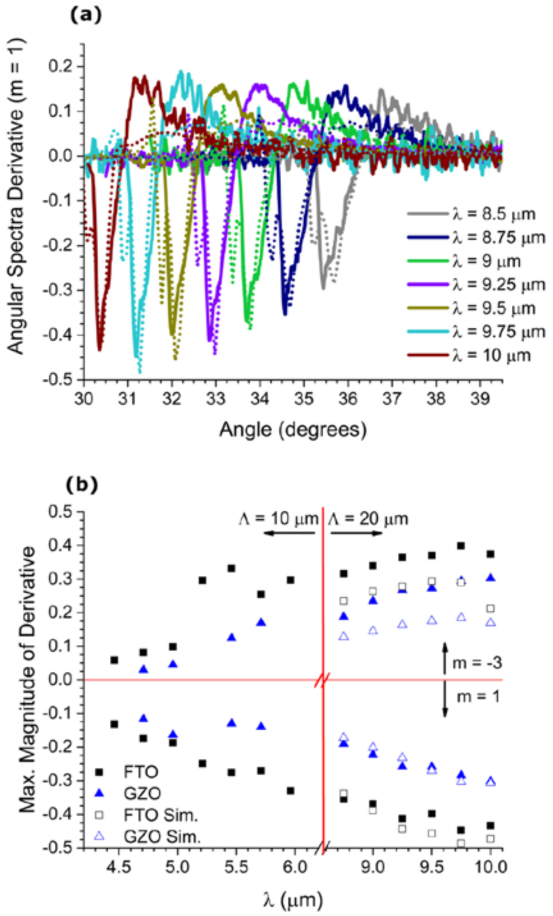

Fig. 6. (a) Derivative of the m = 1 resonance of the FTO grating. Dotted lines are from FDTD simulation while solid lines represent measured data. (b). Maximum magnitude of the derivative for each grating and both m = 1 (bottom) and –3 (top) resonances and for both grating periods, Λ = 10 µm (left) and 20 µm (right). Open symbols represent FDTD simulations while closed symbols represent the measured data.

5. Practical considerations

GZO or FTO can be optimized for a particular application by controlled doping, this also holds for other TCOs such as AZO, ITO, ATO, etc. FTO is not the only TCO that can be spray deposited, but it is the most thermally stable, is the most mechanically and chemically durable, is the least toxic, and is the cheapest of typical TCOs [37]. The conformal nature of spray deposition enables and simplifies fabrication of useful structures such as SPP channel waveguides [38], thus removing etch steps which have proved to be imprecise in materials such as GZO [25]. Moreover, the ability to tune the plasma frequency enables modulators in line with plasmonic waveguides [22, 23, 39], which are also CMOS compatible. Spray-deposited conformal FTO would have applications in band pass filtering on arbitrarily-shaped windows and mirrors.

Considerations for plasmonic materials include the characteristic propagation length and SPP-field penetration into and above the material (see Fig. 2). Useful figures of merit are that SPP intensity propagation length, L_x, should exceed twice the free-space wavelength and that the field penetration depth above the conductor and into the dielectric should be less than thrice λ [13]. For FTO with 1% (actual) fluorine concentration these figures of merit are satisfied in the free space wavelength range 3.53 to 26 µm, which covers most of the MWIR and LWIR regions. The range for GZO (4.75 to 32 µm) is shifted to the red. For perspective, the free space wavelength range gold satisfies these conditions in are 0.5 to 3.0 µm [13]. More information on the propagation lengths and SPP characteristics of MWIR and LWIR of many conductors can found in [40].

A figure of merit recently proposed is $|\chi|^2/\mathrm{Im}(\chi)$ [14], where χ is the electric susceptibility of a material. This figure of merit represents a limit to the absorption, scattering, and electric field enhancement of plasmonic nano- and microstructures regardless of shape, size, and topology. According to this measure FTO and GZO compare favorably to other TCOs such as AZO and ITO [41], but the value of this figure of merit is one order lower for FTO than for noble metals. On the other hand, at MWIR and longer wavelengths, the noble metals structural aspect ratios for optimum plasmonic structures are not currently achievable [14].

6. Conclusion

Photon-to-SPP couplers were fabricated from silicon lamellar gratings conformally coated by spray-deposited FTO. The MWIR and LWIR SPP properties of these gratings were investigated and compared to those of gratings coated with 0.5% GZO, which has similar crossover wavelength, carrier concentration, and resistivity. Experimental and simulated data based on ellipsometry data have been compared. Both experimental and simulation results have been used for validation of a figure of merit based on the angular derivative of the resonance amplitude. This figure of merit allows for accurate determination of the strength of a resonance when other features, such as diffraction edges, are present. Further comparison of FTO to other TCOs and noble metals for MWIR and LWIR are discussed as well as applications for FTO. Conformal FTO coatings are attractive for infrared plasmonic sensing applications and structures that include SPP channel waveguides.

Funding

Air Force Office of Scientific Research (FA9550-15RYCOR162); AFRL.

Acknowledgments

This material is based upon work supported by the Air Force Office of Scientific Research under award number FA9550-15RYCOR162. REP was partially supported as a summer contractor with Wyle Aerospace at AFRL in 2015 and 2016.